Acta Astronautica 218 (2024) 59–69

Contents lists available at ScienceDirect

Acta Astronautica

journal homepage: www.elsevier.com/locate/actaastro

Multibody modelling of tether and capture system for dynamic simulations of In-Air Capturing

Sunayna Singh *, Matteo Mastrogiuseppe

DLR Institute of Space Systems, Linzer Strasse 1, 28359, Bremen, Germany

ARTICLE INFO

Keywords:
Flexible tether dynamics
Large deflection problem
Closed-loop multibody systems
In-Air Capturing
Reusable launch technology

ABSTRACT

The launcher recovery method known as 'In-Air Capturing' is an innovative approach where a winged rocket stage is captured mid-air by an aircraft and subsequently towed back to the launch site. To achieve this, a capturing device attached to a tether is released from the towing aircraft. This device autonomously connects the reusable launch vehicle to the aircraft, while the two vehicles are in proximity. The tether's flexible dynamics have a strong influence on the maneuverability of the capturing device. Thus, it is critical to model the dynamics of the tether to get a realistic understanding and to evaluate feasibility of the concept. However, precise modelling and control of highly flexible systems with large deformations is both challenging and computationally intensive. For engineering applications which involve closed-loop simulations, finding a trade-off between accuracy and computational effort is crucial. In this paper, the tether is modelled as a discretized chain of rigid bodies connected by rotational springs at the joints. The tether along with the capture system is integrated in a simulation model and open loop tests are performed to analyse the system characteristics. The tether properties are studied to find a suited configuration for 'In-Air Capturing'.

1. Introduction

The 'In-Air Capturing' recovery method was first invented and patented by the German Aerospace Center (DLR) in 2003 [1–3]. In this reusable launch technology, a winged booster stage is captured mid-air by a towing aircraft (TA) and towed to the landing site. The aircraft acts as an external propulsion system to the reusable launch vehicle (RLV), eliminating the need for descent propellant. This reduces the overall launch mass and provides potential for considerable cost reduction compared to the current recovery methods like 'downrange landing' and 'return-to-launch site'. A comparitive performance analysis of different RLV approaches and the associated cost benefit against 'In-Air Capturing', can be found in [4] and [5] respectively.

1.1. 'In-Air Capturing' mission cycle

Fig. 1 illustrates the complete operational cycle of 'In-Air Capturing'. During launch, the TA is positioned at a designated downrange rendezvous area. Following the stage separation, the winged booster stage embarks on a ballistic trajectory, quickly descending through the denser atmospheric layers. At approximately 20 km altitude, it decelerates to subsonic speed and descends rapidly in a gliding trajectory. This reusable stage is met by a suitably equipped TA at the rendezvous area around 10 km altitude. Once the two vehicles are in vicinity and gliding in a parallel formation, a capturing device is released from the TA. This device, attached via rope, autonomously spans the distance between the two vehicles and establishes a connection. The entire maneuver occurs at subsonic speeds between 3 km and 8 km altitude. After the successful connection of both vehicles, the winged reusable stage is towed back to the launch site by the larger carrier aircraft. Near the airfield, the stage is released by the TA and autonomously glides to the landing runway.

An essential aspect of 'In-Air Capturing' is the capturing system, comprising of a long tether (up to 350 m) attached to the TA on one end and a capturing device attached to its other end. Given that the capturing device is positioned at the end of a flexible tether, its position and orientation are extremely sensitive to vibrations, perturbations, and general tether dynamics [6,7]. To achieve the capturing of the RLV in a short time (about 70 s), the device must be capable of maneuvering with agility and accuracy [8,9]. Further, the tether model should achieve a balance between computation time and accuracy to facilitate control design and study of closed-loop behaviour. Lastly, the tether properties should be selected, such that it can sustain the loads from towing a large RLV. Thus, the paper aims at modelling and analysis of the tether dynamics and capturing system for the 'In-Air Capturing' of the selected RLV test case.

* Corresponding author.
E-mail address: sunayna.singh@dlr.de (S. Singh).

https://doi.org/10.1016/j.actaastro.2024.02.008
Received 3 November 2023; Received in revised form 26 January 2024; Accepted 7 February 2024
Available online 15 February 2024

Nomenclature

$\mathcal{R}$	Rayleigh damping function
α_t	Total angle of attack
$\boldsymbol{f}$	Inertia forces
$\boldsymbol{M}$	Mass matrix
$\boldsymbol{Q}_D$	Generalized forces due to viscous damping
$\boldsymbol{Q}_i$	Generalized forces on element i
$\boldsymbol{q}_i$	Generalized coordinates of element i
$\boldsymbol{Q}_M$	Generalized forces due to bending moment
$\boldsymbol{Q}_{aero}$	Generalized forces due to rope aerodynamics
$\boldsymbol{Q}_{ext}$	Generalized forces due to external forces
$\boldsymbol{Q}_{rheo}$	Generalized forces due to rheonomous constraints
$\boldsymbol{T}$	Transformation matrix for cartesian coordinates to generalized coordinates
$\boldsymbol{\Phi}$	Relative angular velocity between two elements
ϕ	Generalized rope angle along the horizontal axis
ψ	Generalized rope angle along the vertical axis
k_*	Turbulent kinetic energy
l	Length of a discretized tether segment
m	Mass of a discretized tether segment
n	Number of tether segments
s	Variable representing elongation of rope
u'	Root mean square of velocity fluctuations
u'_A	Component of velocity fluctuation in direction A
U_∞	Free stream velocity

Abbreviations

6DOF	Six Degrees of Freedom
ACCD	Aerodynamically Controlled Capturing Devices
ANCF	Absolute nodal coordinate formulation
DLR	German Aerospace Center
FEM	Finite element method
RANS	Reynolds Averaged Navier–Stokes
RLV	Reusable launch vehicle
TA	Towing aircraft
UHMWPE	Ultra-High-Molecular-Weight Polyethylene

1.2. State of the art

Considering only elastic deformation in the tether (constant stiffness), a number of modelling approaches can be explored. Some common models used for the simulation of tethers and cable-like bodies are based on continuum mechanics, multibody approaches (liked lumped mass models) and finite element method (FEM) [10–25]. Based on the mission heritage of systems similar to 'In-Air Capturing', closer associations can be made for the application. Both aerial and underwater towing systems contain a larger vehicle (aircraft or ship) towing a smaller vehicle (*e.g.* drone, submarine) via cables or tethers. Most of these applications require accurate positioning of the tip [14–18]. Huffman and Genin [14] performed several studies on the dynamics of a sphere towed by an aircraft, using continuum mechanics for the modelling of the cable. In the work of Kamman et al. [15,16], both aerial and underwater towed flexible cable systems are modelled using rigid links connected by frictionless hinges and lumped masses, forces concentrated at joints. Williams et al. [17,18] model an aerial towing system using lumped masses attached via spring to each other. Lastly, Morozov [19] models the cable dynamics for aerodynamic design of the towed aircraft, in order to achieve a favourable equilibrium position.

Another technology that shares heritage with 'In-Air Capturing', is the aerial refuelling system. It commonly consist of a flexible refuelling hose attached to a tanker aircraft and a drogue at the end of the hose. A popular methodology appears to be multibody models with rigid links connected by spherical joints [16,18,20–22]. Both continuum [24] and classical FEM models [25] have also been used for modelling of aerial refuelling systems, providing good accuracy but with large computational effort [12]. A variation of FEM called absolute nodal coordinate formulation (ANCF) has recently gained recognition for the possibility of producing accurate results for large deformation problems with lower computation effort than FEM [26,27]. Nonetheless, lumped parameter multibody models are often preferred due to the simplicity of modelling and versatility [12]. Thus, a multibody approach proposed by Fritzkowski and Kaminski [28–30], is chosen for the modelling of tether in 'In-Air Capturing' application. The approach provides a good trade-off between ease of implementation, computation effort and accuracy [31]. The methodology assumes that the tether can be divided into equal rigid segments connected to each other by spiral springs.

1.3. Outline of the paper

To understand the requirements of the 'In-Air Capturing' system, first the two large scale vehicles are briefly introduced in Section 2. For appropriate modelling of the capture system, the capturing device and its properties are discussed in Section 2.1. Next, the perturbing forces originating from the wake of the aircraft are analysed and modelled. Then, the modelling of the rope is presented in Section 2.3. All the subsystems are then combined in the definition of equations of motions of the system given in Section 3. The constraints, boundary conditions and assumptions applied to modelling are also discussed in this section. Different tether characteristics are evaluated using sensitivity studies and a suitable configuration is selected for future closed-loop simulations of 'In-Air Capturing'. Lastly, some conclusions and future work are presented in Section 5.

2. In-air capturing system

As shown in Fig. 2, the capturing system consists of the tether attached to the TA on one end and the capturing device on the other end. To comprehend the requirements for the tether as well as the capturing system, some background on the vehicles involved in 'In-Air Capturing' is required. In this study, two large scale test cases were selected.

- *Reusable Launch Vehicle (RLV)*: To achieve extended formation flights with a high-performance aerodynamic aircraft, it is essential for the RLV to be equipped with wings. This design choice requires an increased Lift-to-Drag (L/D) ratio in the RLV. However, a substantial wingspan in RLVs may result in shock–shock interactions during re-entry. Consequently, a configuration featuring foldable outer wings has been chosen. Fig. 3 illustrates the reusable launcher stage, designated RLVC4. Further details about the vehicle can be found in [8,32]. A descent weight of 80 tons is estimated based on the current design.
- Towing Aircraft (TA): The retired jetliner Airbus A340-600 [33] is selected as the TA due to its large loading capacity and thrust. The A340-600, equipped with four robust Rolls-Royce Trent 556 engines and an advanced flight control system, aligns with the specifications for 'In-Air Capturing' of the large RLV. Opting for this long-range commercial aircraft also brings the advantages of cost-effectiveness in acquisition and promotes reusability, making it a practical choice for the task. Some detailed design requirements and modifications for the TA involved in 'In-Air Capturing' are described in [8].

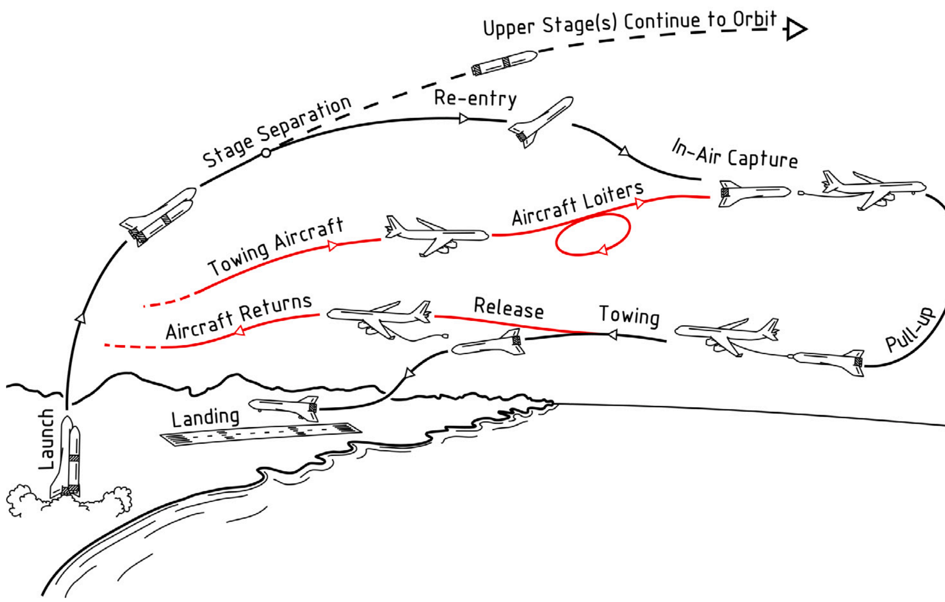

Fig. 1. Schematic of the complete 'In-Air Capturing' mission cycle.

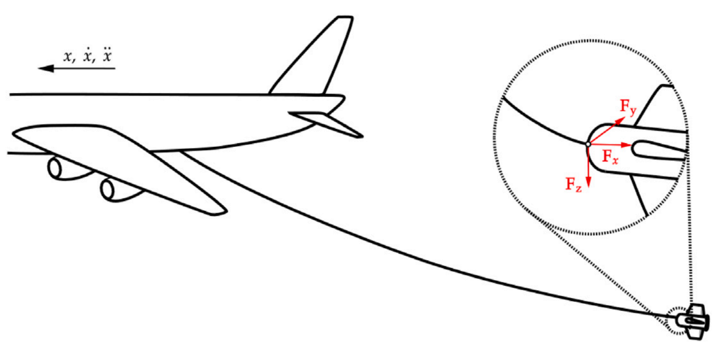

Fig. 2. Schematic of capturing system with TA, tether and capturing device.

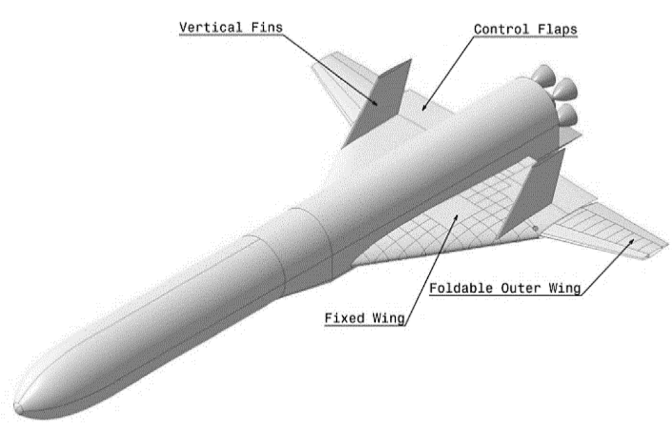

Fig. 3. Reusable launcher stage - RLVC4.

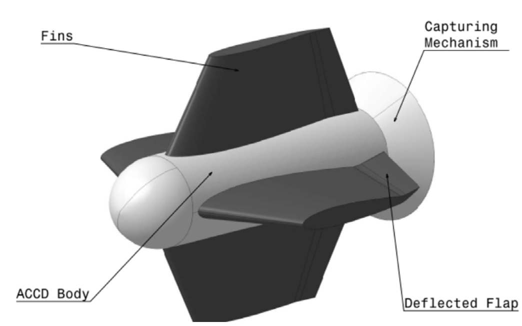

Fig. 4. ACCD Geometry with fins and capturing mechanism.

Thus, with the goal of capturing RLVC4, this section summarizes the modelling methodology of the essential subsystems in the capturing system of 'In-Air Capturing'. For the current study, it is assumed that the TA flies with a constant velocity of 185 m/s and an altitude of 6000 m. Next, the preliminary design and operating principle of the capturing device is discussed. Since the device trails behind the TA during capture, the modelling of external disturbances from aircraft wake is also presented. Lastly, a multibody approach is presented for efficient modelling of the flexible dynamics of the tether.

2.1. Aerodynamically Controlled Capturing Device (ACCD)

Based on earlier research performed at DLR, the Aerodynamically Controlled Capturing Devices (ACCD) was identified as the most promising capturing technique for 'In-Air Capturing' [34]. This device demonstrated superior performance and agility while presenting the lowest level of risk. Fig. 4 provides a schematic representation of the ACCD, which measures 2 m in length with a cross-sectional diameter

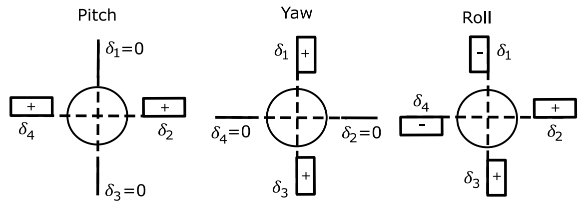

Fig. 5. ACCD flap deflections and resulting moments (from behind).

of 1.5 m, including the fins. It features four flaps capable of deflecting up to a maximum of ±15°, providing Six Degrees of Freedom (6DOF) agility and control. The ACCD's nose is connected to the TA via a tether, and the capturing mechanism is included at the rear of the ACCD. It establishes a secure connection using a lock-in mechanism with a boom on the RLV.

Fig. 5 illustrates how roll, pitch, and yaw deflections are achieved through the movement of the four flaps. For pitch maneuvers, both horizontal flaps deflect in the same direction, while for yaw adjustments, both vertical flaps move in the same direction. For roll motion, all flaps deflect as shown in Fig. 5. Asymmetric flap deflections facilitate movement in more than one direction, using a superposition approach proposed in [35]. The symmetric configurations of flap deflections, up to 10° for pitch, yaw, and roll motion, were examined through Reynolds Averaged Navier–Stokes (RANS) computations, covering a range of ±15° angle of attack. This analysis aimed to gain a better understanding of the ACCD's aerodynamic performance and stability characteristics [7]. The data obtained from these simulations is subsequently utilized in the dynamic simulations of 'In-Air Capturing'. From the analysis, it was concluded that the current ACCD design remained statically stable. Further details on simulation specifications and in-depth aerodynamic analysis can be found in [7,36].

2.2. Aircraft wake

Based on a detailed study of aircraft wake documented in [8], it was determined that the wake exhibits a significant vertical (downwash) component, particularly at higher angles of attack. Fig. 6 shows the velocity contour of the wake trailing behind the TA generated using RANS. The simulations employed a steady state solver (rhoSimpleFoam), which simplifies the approximation of turbulence compared to the intricate patterns commonly observed in a wake. However, for this particular study, the simplified model adequately captures the characteristics of the wake. Specific simulation parameters for the CFD study can be found in [7]. From Fig. 6, it becomes evident that variations in velocity due to the wake are considerable even at a distance of 315 m from the nose of the aircraft. Given that the ACCD is required to trail behind the aircraft during the capture phase, its exposure to the wake is very likely. Furthermore, the aircraft is expected to operate at high angles of attack during the descending flight [8], subjecting the ACCD to substantial disturbances. Consequently, it is imperative to analyse these effects in controlled flight simulations of the ACCD.

Fig. 7 shows the wake velocity profiles within the fuselage plane, expressed as a fraction of the free-stream velocity (U_∞). The distances from the aircraft in both the horizontal (X) and vertical (Z) directions are scaled using the aircraft's length (L =70 m). It can be observed that the streamwise (horizontal) velocity component diminishes with increasing distance from the TA and is confined within a width of $z/L = \pm 0.25$. However, the downwash (vertical) velocity component persists even as the distance from the aircraft grows, enveloping a width of $z/L > \pm 0.50$ from the aircraft's nose. For an angle of attack of 8°, this downwash component (U_z) was found to reach approximately 8% of the free-stream velocity, even at a distance of 315 m from the aircraft. This presents a substantial challenge in control of the ACCD, as the device encounters continuously changing velocity and turbulence. Consequently, these factors can lead to disturbances in its angle of attack, impacting pitch maneuvers.

In the current system, the wake is modelled as a change in free-stream velocity based on the position of the ACCD behind the TA. The turbulence due to wake is added as time dependent velocity fluctuations given by the formula [37]:

$$u' = \sqrt{\frac{1}{3}({u'_x}^2 + {u'_y}^2 + {u'_z}^2)} = \sqrt{\frac{2}{3}k_*} \tag{1}$$

Here, u' represents the root mean square of velocity fluctuations (u'_x, u'_y, u'_z) resulting from turbulence. k_* represents the turbulent kinetic energy, which is obtained from the RANS simulations. The wake module utilized in the simulation incorporates look-up tables. These tables generate alterations in the free stream velocity based on the ACCD's position behind the aircraft. To imitate the turbulence, time-dependent velocity fluctuations are incorporated into this data.

2.3. Tether modelling

The general idea for the tether modelling is taken from the work of Fritzkowski et al. [28–30]. However, the discretized tether model presented in [28–30] is in 2D, which is insufficient for the current application. Hence, the methodology is extended to 3D and adapted for 'In-Air Capturing' simulations. Here, one end of the tether is attached to the aircraft and is constrained by its motion. Therefore, the origin of the global reference frame for the tether is assumed at the attachment point of the TA, effectively enforcing a fixed joint constraint. This approach enables the description of the tether's relative kinematics with respect to the TA. When the TA maintains a constant velocity, the reference frame becomes inertial. In this simplified scenario, there is no need to introduce inertia forces in the tether model. However, during 'In-Air Capturing', the TA can decelerate or accelerate to align with the RLV. Consequently, the origin is modelled as a moving support, for which the position is time dependent. These constraints are further explained in Section 2.3.5.

The tether is discretized into n identical segments of length l and mass m each, connected by identical massless springs of stiffness k_t. Assuming that each element behaves like a rigid cylindrical rod, the discrete model of the tether resembles a system of 3D multiple pendulum system. Thus, the current model includes two generalized angles, ϕ and ψ to define the relative displacement along the horizontal and vertical directions respectively. As shown in Fig. 8, a spherical coordinate approach is adapted. The Cartesian position (x_1, y_1, z_1) of a point P_1 can be obtained as follows:

$$\left.\begin{aligned} x_1 &= l \cdot \cos\psi_1 \cdot \sin\phi_1 \\ y_1 &= l \cdot \cos\psi_1 \cdot \cos\phi_1 \\ z_1 &= l \cdot \sin\psi_1 \end{aligned}\right\} \tag{2}$$

Considering a chain of bodies, the Cartesian coordinates of the ith element (considering local frame at the centre of mass) can be written as follows:

$$\left.\begin{aligned} x_i(t) &= x_0(t) + \frac{l}{2}\sum_{j=1}^{i-1} \cos\psi_j \cdot \sin\phi_j + \frac{l}{2}\cos\psi_i \cdot \sin\phi_i \\ y_i(t) &= y_0(t) + \frac{l}{2}\sum_{j=1}^{i-1} \cos\psi_j \cdot \cos\phi_j + \frac{l}{2}\cos\psi_i \cdot \cos\phi_i \\ z_i(t) &= z_0(t) + \frac{l}{2}\sum_{j=1}^{i-1} \sin\psi_j + \frac{l}{2}\sin\psi_i \end{aligned}\right\} \tag{3}$$

The components of the linear velocity ($v_i(t)$) and acceleration ($a_i(t)$) of the ith segment in the *X, Y, Z* directions are computed simply as the numerical derivative of the position (Eq. (3)) with respect to time. Detailed description of these equations can be found in [31]. For a comprehensive dynamic modelling of the system, a number of internal and external factors need to be studied. These will be explained in the coming subsections.

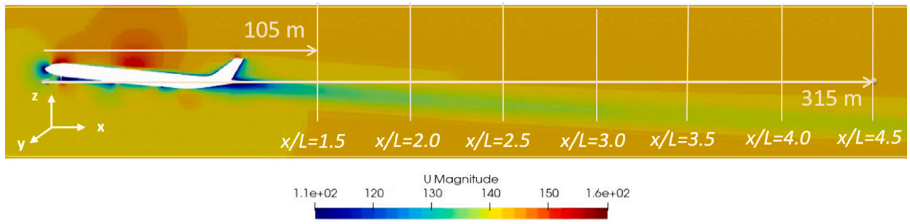

Fig. 6. Velocity contour of the wake behind the aircraft [8].

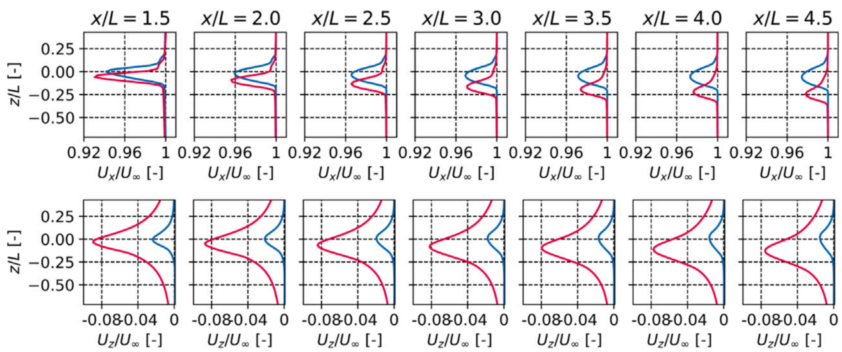

Fig. 7. Wake profiles in the fuselage plane for 0° (blue) and 8° (red) angle of attack; streamwise velocity (top) and downwash velocity component (bottom) [8].

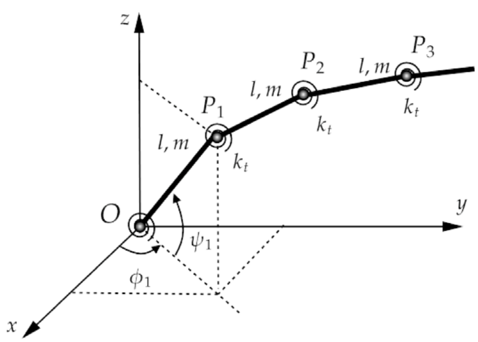

Fig. 8. 3D definition of tether segments using spherical angles.

2.3.1. Bending stiffness

In the current model, identical, massless springs with stiffness k_t are placed at each joint, as shown in Fig. 8. These elements apply a torque opposite to the curvature of the tether (R). The associated bending moment M is computed using the expression:

$$M = \frac{k_t}{R} \tag{4}$$

Non-linear springs with changing flexural rigidity (k_t) are considered to avoid unnatural full rotations at the joints. In other words, if two elements tend to have a relative rotation such that $\phi_1 - \phi_2 = \pi$, the elastic force M will grow infinitely. The related generalized forces (Q_i^M) associated with the polar angle ϕ_i can then be written as:

$$\boldsymbol{Q}_i^{\boldsymbol{M}} = \begin{cases} M_i - M_{i+1}, & \text{for } i = 1, 2, \ldots, n-1 \\ M_i, & \text{for } i = n \end{cases} \tag{5}$$

This process [28] is also followed in 3D, where calculations for generalized forces are performed independently for angles ϕ and ψ (refer to Fig. 8).

2.3.2. Viscous damping

Springs alone are not sufficient to stabilize the dynamics of the system [30]. Thus, viscous dampers with damping coefficient c are added to the tether joints. For a generalized coordinate angle ϕ, dissipative generalized forces may be derived from the Rayleigh dissipation function:

$$\mathcal{R} = \frac{1}{2} c \sum_{i=1}^{n} \dot{\boldsymbol{\Phi}}_i^{\,2} \tag{6}$$

where $\dot{\boldsymbol{\Phi}}_i$ represents the relative angular velocity between two elements ($\dot{\phi}_i - \dot{\phi}_{i-1}$). The generalized forces for viscous damping are then given by:

$$\boldsymbol{Q}_i^{\boldsymbol{D}} = -\frac{\partial \mathcal{R}}{\partial \dot{\phi}_i} = \begin{cases} c\left(\dot{\boldsymbol{\Phi}}_{i+1} - \dot{\boldsymbol{\Phi}}_i\right) & \text{for } i = 1, 2, \ldots, n-1 \\ -c\,\dot{\boldsymbol{\Phi}}_i & \text{for } i = 2, 3, \ldots, n \end{cases} \tag{7}$$

The damping coefficient c is derived from the simple empirical assumption of Rayleigh Damping [10]. The damping coefficients depend strongly on the tether properties and often can only be correctly estimated through experiments [38]. Since no experiments were possible during this study, an estimation is done through generic benchmark test cases [39,40] and stable tether behaviour. More details about the coefficients can be found in [31].

2.3.3. External forces

The external forces are modelled to account for the forces applied by the ACCD on the last node as shown in Fig. 2. This includes the aerodynamic forces, gravity and disturbances from the wake acting on ACCD. A detailed study on aerodynamic properties of the capturing device can be found in [7,35]. This total external force can be translated into generalized coordinates to be integrated with the rope model.

$$\boldsymbol{Q}_{ext} = \boldsymbol{F}_{ext} \cdot \mathbf{T} \tag{8}$$

where T is the transformation matrix for cartesian coordinates to the generalized coordinates of the system.

2.3.4. Aerodynamics

In the context of the 'In-Air Capturing', a drag model must be applied to the tether body. Aerodynamic effects are analysed by describing tether elements individually. The drag (C_D) and lift (C_L) coefficients as a function of the angle of attack of the body, were estimated using J. H. Lee's work, which describes the dynamics of tethers in underwater structures [41]. Since the current tether model

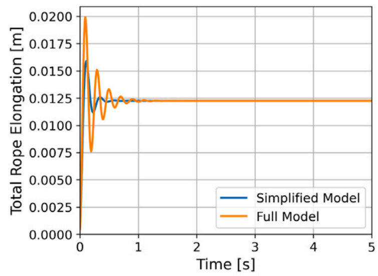

(a) Elongation under tether weight

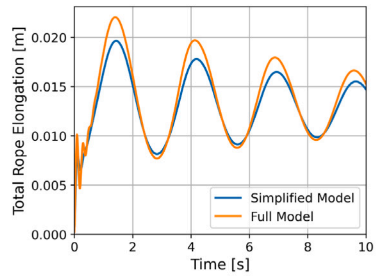

(b) Elongation during swing

Fig. 9. Comparison of elongation approaches.

Table 1
Simulation parameters for tether elongation.

n	L [m]	m_{tot} [kg]	k [N/m]	$c1$ [N m s/kg]
4	10	5	10 000	20

describes the position in 3D, the effect of both angles ϕ and ψ should be considered for the aerodynamics. Therefore, a total angle of attack (α_{tot}) is considered [42]. Since the element orientation is described using spherical coordinates, the velocity can be written as a function of free-stream velocity (U_∞).

$$\begin{aligned} u &= U_\infty \cdot \cos\alpha_t \\ u &= U_\infty \cdot \cos\phi \cdot \cos\psi \end{aligned} \quad \rightarrow \alpha_t = \cos^{-1}(\cos\phi \cdot \cos\psi) \tag{9}$$

The aerodynamic forces, expressed in Cartesian components, must also be transformed into generalized forces (Q_{aero}) using the same process shown in Section 2.3.3.

2.3.5. Rheonomous constraints

In the current model, the reference frame of the tether is described relative to the position of the TA, and its origin is fixed in the connection point. Hence, the origin of the tether reference frame is constrained to have the same motion as the TA. This acts like a *rheonomous constraint* for the system, because the time variable appears explicitly in the equation [28]. In the final set of equations, the contribution of rheonomous constraints to the non-Lagrangian of the system is:

$$\boldsymbol{Q}_{rheo} = -m\boldsymbol{a}_0(t) \tag{10}$$

where $a_0(t)$ is the acceleration of the tether's first node. It can be visualized as an apparent inertia force applied to all elements that acts in the opposite direction to the reference frame acceleration. In the 'In-Air Capturing' mission, the TA reference frame cannot be considered as inertial, if it undergoes any acceleration. Therefore, to maintain this constraint and simulate the effect of TA acceleration, the apparent forces are applied to the tether model.

2.3.6. Tether elongation

Another goal of the study is to find tether characteristics that can sustain the loads from towing of RLV. Therefore, the model must also look into the tether tension and elongation. In the work of Fritzkowski [28–30], simple 2D model of the tether is expanded, by using axial spring-damper elements at every joint. However, maintaining system stability within a reasonable computation time becomes challenging with this model. These challenges are further amplified as the model is extended to 3D. As a consequence, a simplified model is proposed. A linear visco-elastic element is introduced at the beginning of the chain instead of every joint. This component is assumed to model the elongation of the whole tether, using the axial stiffness (k) and damping ($c1$).

Simple verification tests are performed to check the validity of assumption. The test case is simply a 3D extension from the test case used in [28–30]. A 10 m long tether (fixed at one end) is assumed with specifications as shown in Table 1. Fig. 9(a) shows the elongation of a vertical tether extending under its own weight. The 'full model', with springs at every joint (considering 4 elements), appears to have larger amplitude of oscillations compared to the 'simplified' model with one spring. A similar observation can be made in Fig. 9(b), which shows the same tether swinging under its own weight, when released from an initial point ($\phi = \pi/4$ and $\psi = \pi/4$). Although the simplified model is able to capture the oscillatory motion with lower computational effort, it is less accurate. Tuning of stiffness and damping factors of the simplified elongation model through experiments can improve accuracy. Nonetheless, a factor of safety is considered during the estimation of maximum tension in the tether.

Taking into account all modelling and assumptions, the tether modelling approach has been verified through several test cases derived from Fritzkowski's research [28–30]. The test cases replicated the dynamics of the reference system and adhered to the law of conservation of energy. The verification cases can be found in [31].

3. System integration

In this section, the previously described subsystems are integrated and the dynamics of the system are defined. Since the goal of the simulation is to determine the position of the ACCD behind the TA, the dynamics of the system can be visualized using the simplified representation shown in Fig. 10. The origin of the coordinate system that marks the first node of the tether, is assumed to be attached to the TA. An axial spring-damper system is considered at the first node (attachment point) for estimation of elongation in the tether. This is followed by a chain of identical rigid elements connected by angular spring-damper systems. Finally, a lumped mass equivalent to the mass of the ACCD is considered at the end node (free end) of the tether. In the current study, torsional moments due to the tether were not included. Therefore, the ACCD is assumed to be attached to the last node via a spherical joint at the center of gravity. In such a scenario, only the translational motion of the ACCD is affected by the tether. The rotational motion is assumed to be independent of the tether. Based on these assumptions, the equations of motions are defined and the simulation environment is set up.

3.1. Equations of motion

To derive the translational equations of motion, the Euler-Lagrangian approach is used. The Lagrange equations of motion can be written as [10]:

$$\frac{d}{dt}\left(\frac{\partial \mathcal{L}}{\partial \dot{q}_i}\right) - \frac{\partial \mathcal{L}}{\partial \boldsymbol{q}_i} = \boldsymbol{Q}_i, \quad i = 1, 2, \dots, n \tag{11}$$

where $\boldsymbol{Q}_i$ are the generalized forces (also referred to as non-Lagrangian components) applied to the system. The number of equations per tether

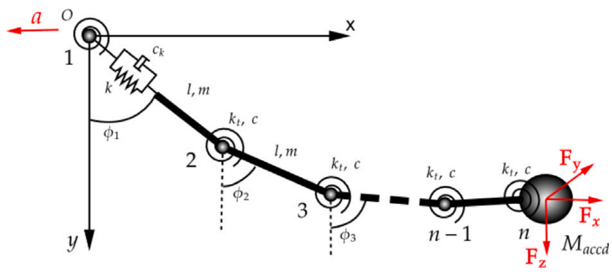

Fig. 10. Schematic of the integrated TA-Tether-ACCD system.

segment is equal to number of generalized coordinates (q_i) used in the description of the chain. Two angles (ϕ and ψ) as shown in Fig. 8 are used to characterize each element. Additionally, an elongation variable s is also included. Hence, the number of variables will be $2n+1$ in total. The final equations of motion take the following form:

$$\boldsymbol{M}(\boldsymbol{q})\ddot{\boldsymbol{q}} = \boldsymbol{f}(t, \boldsymbol{q}, \dot{\boldsymbol{q}}) + \boldsymbol{Q}_D + \boldsymbol{Q}_M + \boldsymbol{Q}_{aero} + \boldsymbol{Q}_{rheo} + \boldsymbol{Q}_{ext} \tag{12}$$

where:

$$\boldsymbol{M}(\boldsymbol{q}) = \begin{bmatrix} M_{1,1} & M_{1,2} & \cdots & M_{1,k} \\ M_{2,1} & M_{2,2} & \cdots & M_{2,k} \\ \vdots & \vdots & \ddots & \vdots \\ M_{k,1} & M_{k,2} & \cdots & M_{k,k} \end{bmatrix}, \quad \boldsymbol{f} = \begin{bmatrix} f_1 \\ f_2 \\ \vdots \\ f_k \end{bmatrix}$$

k is the total number of variables in the system, equal to $2n+1$. The detailed expressions for the mass matrix ($\boldsymbol{M}(\boldsymbol{q})$) and inertia terms ($\boldsymbol{f}$) are given in Appendix. The generalized forces on the right hand side were explained in Section 2.3.

3.2. Simulation environment

Using the equations of motion stated above, a simulation set up for the capture system is built. Fig. 11 briefly describes the tether sub-module as a part of the full-scale simulation architecture. The complete simulation architecture for 'In-Air Capturing' can be found in [7]. The tether model is essentially a function that computes the translational equations of motion of the capturing device (end node of the tether). The simulink block requires a set of inputs:

- *TA acceleration*: Since the tether shares the top node with the aircraft, accelerations in the TA motion will generate apparent forces as shown in Eq. (12). Thus, the Cartesian coordinates of the TA acceleration are input to the model.
- *External Forces*: In the context of application, the ACCD is included as a lumped mass at the end of the tether (as shown in Fig. 10). Hence, this input accounts for the aerodynamics, gravity or any other forces acting on the capturing device. Distributed forces like gravity and aerodynamics of the tether are handled internally in the tether model and do not require any inputs.
- *Tether Specifications*: Here the tether properties like length, diameter, material, mass *etc.* are defined.

The 'Equations of Motion' subsystem block outputs the derivative of the state, which is fed to an ODE solver. Initial conditions for the system, in the form of tether angles and elongation, are provided. The final output of the integrator is the translational position and velocity of the capturing device (last node of the tether). In the coming section, open loop tests will be performed by varying the tether properties and external forces coming from capturing device, to study the system characteristics.

Table 2
Material properties of different tethers [44–46].

Material	Diameter [mm]	Mass per unit length [kg/m]	Maximum Tension [kN]
UHMWPE	16	0.156	280
UHMWPE	24	0.329	550
UHMWPE	32	0.555	900
Kevlar	16	0.156	175
Kevlar	32	0.555	578
Steel	24	2.34	375
Steel	32	4.1	645

4. Open loop simulations

The tether properties contribute significantly to the dynamics of 'In-Air Capturing' and thus, must be carefully selected. To ensure effective maneuverability of the capturing device, the tether should be lightweight. It is equally crucial for the tether to possess the strength necessary to withstand towing forces once the RLV is attached. Thus, the material, length and diameter of the tether must be selected accordingly. Further, factors like disturbances from wake, must also be considered during the tether design. Consequently, a sensitivity study is conducted to evaluate the most suitable tether configuration. A simple set of open-loop control commands, encompassing pitch and yaw adjustments (as illustrated in Fig. 12), are employed to assess the maneuvering capabilities of the capturing device. The system is directed to execute pitch maneuvers and yaw maneuvers by deflecting its flaps. For the current test simulation, the aircraft is assumed to be in a cruise state, with constant velocity (185 m/s) and altitude (6000 m). The initial tether configuration is set to be straight ($\phi = 0$ and $\psi = \pi/2$), tensed and horizontal with respect to the plane. An Runge–Kutta fourth order fixed step integrator with a timestep of 10^{-2} is used.

4.1. Tether material

The first criteria for selection of a suitable tether material is the tether's maximum allowable tension. It is crucial to guarantee that the tether is able to sustain the maximum tension scenario during the mission as shown in Fig. 13. This occurs when the RLV is already connected to the capturing system and flying with maximum drag. The airplane's engines are throttled up to maximum thrust while the TA is flying with minimum drag. The TA is considered to be the long-range jetliner A340-600 with four engines [8]. Each of these engines is expected to provide a maximum thrust of 260 kN when at sea level [33]. At the same time, the RLV [43], with a mass of approximately 80 tons is attached to the other end after the successful capture. Assuming that the RLV lift is balanced by its weight, the maximum drag is estimated to be about 50 kN. To simulate this scenario, associated forces are applied on the ends of the tether and the maximum tension is evaluated.

Fig. 14 shows the tension in the tether in the maximum tension scenario. In steady-state conditions, the stress oscillates around 125 kN and peaks at approximately 225 kN. Since an accurate estimation of this tension is not possible with the current model (as explained in Section 2.3.6), a factor of safety of 3 is considered. Thus, the tether for 'In-Air Capturing' application must have a maximum allowable tension that is higher than 450 kN. Table 2 summarizes the maximum allowable tension and mass of different diameters of Ultra-High-Molecular-Weight Polyethylene (UHMWPE) and Kevlar tethers compared against some standard steel wire tethers. It can be observed that UHMWPE tethers offer the highest strength with the lowest mass per unit length.

UHMWPE (also known as Dyneema) is renowned for its high strength and minimal stretching properties. One significant advantage of UHMWPE tether is that it can replace a steel wire tether of the same diameter at only 1/7th the weight [46]. These tethers are lightweight and possess the added benefit of vibration damping properties.

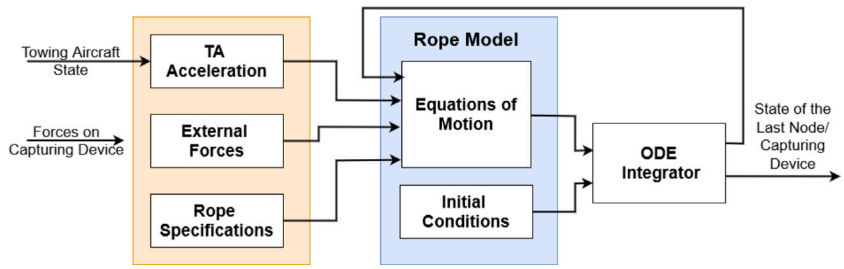

Fig. 11. Scheme of the simulation environment.

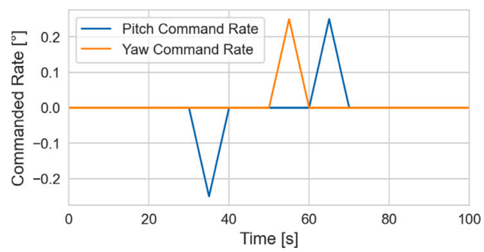

Fig. 12. Open loop control rates for sensitivity study.

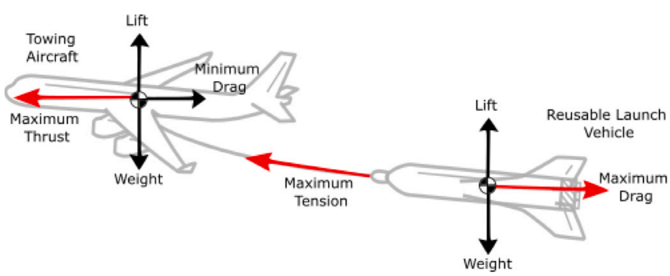

Fig. 13. Forces for maximum tension in tether after the successful capture of RLV.

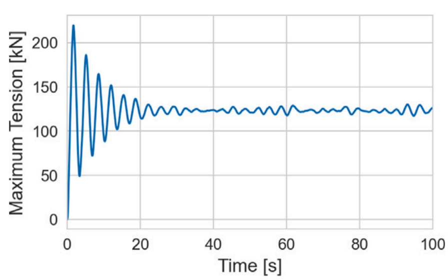

Fig. 14. Maximum tension in tether due to RLV drag.

Based on Table 2, it can be concluded that, a minimum diameter of 24 mm is required to meet the strength requirements for 'In-Air Capturing' application. For the same diameter, UHMWPE tethers are comparatively lighter and offer higher breaking strength. To understand the effect on dynamics, UHMWPE and steel tethers of 250 m length and 24 mm diameter are considered in dynamic simulations. Fig. 15 shows the relative equilibrium position of the capturing device behind the TA. No control deflections are applied and the vibrations in tether are allowed to dampen naturally. It can be observed that the Steel tether being much heavier, settles more than 100 m below the TA and oscillates for a longer duration. The lighter UHMWPE tether settles quickly and stabilizes to about 50 m below the aircraft. Thus, a UHMWPE clearly provides superior performance and is examined further for the 'In-Air Capturing' application.

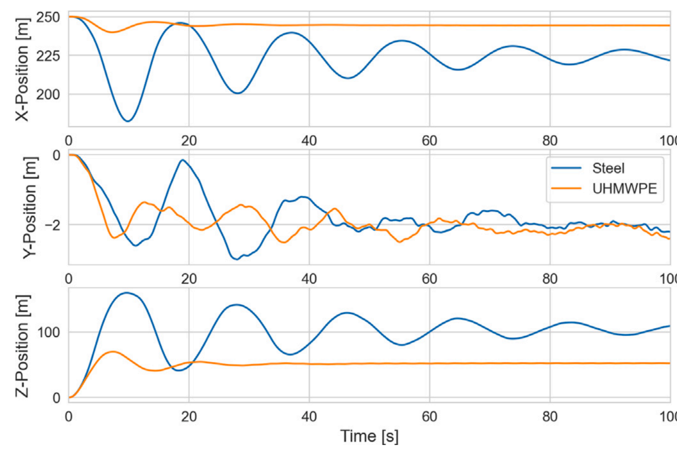

Fig. 15. Sensitivity to tether material — Steel and UHMWPE.

4.2. Sensitivity to length

Tether length is another variable that can influence the system's behaviour. A shorter tether might exhibit restricted maneuverability, while longer tethers tend to be heavier and could generate more pronounced vibrations that take longer to dissipate. Additionally, longer tethers may necessitate a finer level of discretization to accurately model their dynamics, leading to increased computational demands. To explore the impact of tether length, an open loop test is conducted using the commands illustrated in Fig. 12. A 24 mm diameter UHMWPE tether with 30 tether segments is considered. Figs. 16(a) and 16(b) shows the relative position of the capturing device behind the aircraft. It can be observed that the 300 m long tether results in more significant movement (especially in Z-direction) compared to the shorter tether of 150 m. However, this longer tether also exhibits greater amplitude in vibrations and has extended settling times. This heightened vibration amplitude could hinder the system's maneuverability by requiring lengthier settling periods, potentially limiting the capturing device's ability to execute multiple corrective maneuvers during the capture of the RLV.

Taking a closer look at the vertical displacement (Fig. 16(b)), it becomes evident that heavier and longer tethers tend to stabilize at a lower position in the Z-direction, approximately 70 m below the reference point for the 300 m tether. This characteristic may prove advantageous in terms of exposure to wake disturbances since shorter tethers stabilize very close to the wake [43]. Fig. 17 show the response of the longer tethers (250 m and 300 m) when exposed to the wake. It can be observed that both ropes are similarly affected by wake and a major advantage of selecting a longer rope is not evident. Therefore, considering the trade-off between reduced computational effort, faster settling times and wake exposure, an intermediate tether length of 250 m is analysed.

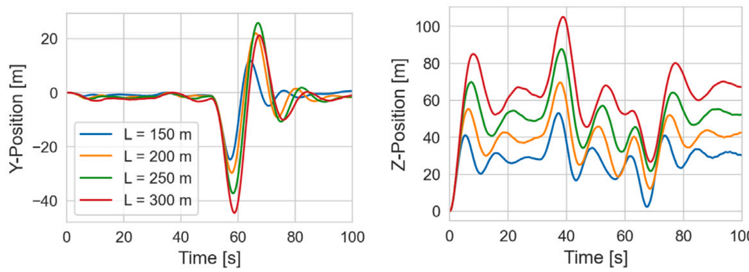

(a) Lateral displacement of tether end (b) Vertical displacement of tether end

Fig. 16. Open loop response of tether to different tether lengths.

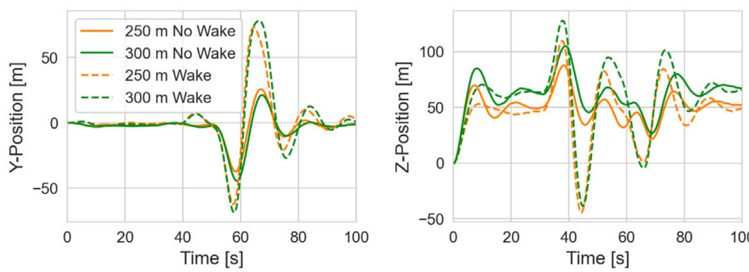

(a) Lateral displacement of tether end (b) Vertical displacement of tether end

Fig. 17. Open loop response of tether to different tether lengths with wake exposure.

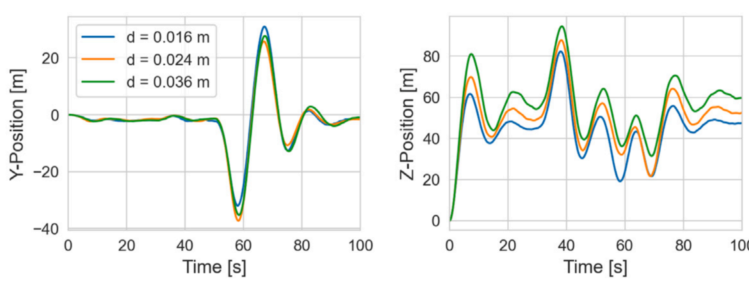

(a) Lateral displacement of tether end (b) Vertical displacement of tether end

Fig. 18. Open loop response of tether to different tether diameters.

4.3. Sensitivity to diameter

Here, the tether behaviour for different tether diameters and a fixed length of 250 m is analysed. In this scenario, when the diameter is doubled, the tether's weight increases nearly fourfold. Both bending and axial stiffness also increase significantly, resulting in a notably rigid tether. This increased stiffness can have contrasting effects on the system's behaviour. On one hand, a stiffer tether may reduce the amplitude of vibrations transmitted through the tether. Conversely, it has the potential to significantly diminish the maneuverability of the capturing device. Thus, an open-loop test is been conducted using the fundamental commands outlined in Fig. 12, to assess the system's maneuverability and stability.

Figs. 18(a) and 18(b) show that vibrations are more pronounced when using larger tether diameter. Consequently, these vibrations also exhibit a prolonged duration before damping out. This can be attributed to the fact that a thicker diameter results in a stiffer tether. When subjected to the same pitch command (as shown in Fig. 12), it becomes apparent that for a 16 mm diameter tether undergoes larger displacement. A similar trend can be observed in the lateral direction, where the capturing device exhibits greater mobility with the 16 mm diameter tether. Thus, it can be concluded that a heavier tether diminishes the maneuverability of the capturing device. However, as mentioned in Section 4.1, a minimum of 24 mm diameter must be considered for sufficient breaking strength. Thus, the tether model with a 24 mm diameter is selected for further studies.

Table 3
Simulation parameters for selected tether for 'In-Air Capturing' simulations.

n	L [m]	m_{tot} [kg]	k [N/m]	k_t [N m^2]	$c1$ [N m s/kg]	c_k [N s/m kg]
30	250	82.25	157 431.5	170	1	100

Based on the sensitivity study, the selected tether properties are summarized in Table 3. Fig. 19 shows the relative equilibrium position of the capturing device behind the TA. The capturing device is released from a horizontal position behind the aircraft is allowed to settle (no fin deflections). It can be observed that the capturing device settles to about 50 m below the aircraft, as the vibrations from tether dampen out over a period of approximately 40 s. Thus, the simulation remains stable even with relatively large fixed-timesteps (10^{-2}). Future 'In-Air Capturing' trajectory simulations will thus be performed using the developed tether model and the selected tether characteristics in this study.

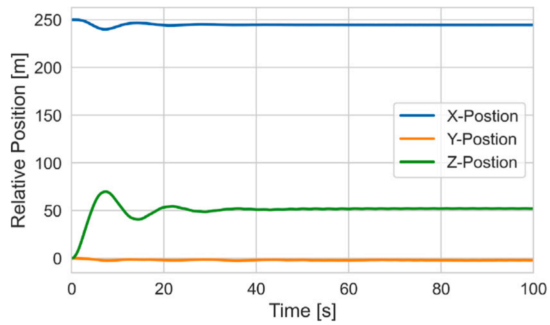

Fig. 19. Open loop response for the selected tether characteristics.

5. Conclusions and future work

In 'In-Air Capturing', a winged launcher stage is recovered mid-air by an aircraft and towed to the landing site. The capture is achieved through a capturing system, which consists of a tether attached to the aircraft on one end and a capturing device on the other end. Hence, the success of capture relies strongly on the accurate positioning of the tether end. In this study, the tether is modeled as rigid links connected by spiral springs. The capturing system including the capturing device is modeled relative to the towing aircraft. The constraints and boundary conditions in the equations of motion are applied to fit the 'In-Air Capturing' application. Simplifying assumptions are made to reduce computational effort. The integration of the capturing system with the full-scale model as well as selection of appropriate tether properties are also presented in the work.

The current model does not take into account twisting effect of the tether. Future work would extend the model to 6DOF system by including the torsional stiffness in the tether model. Another important aspect that must be further examined in future is the coupling between the bending stiffness along XY and XZ planes. Next, the tether model should be tuned and validated through lab experiments. Further improvements can be made to the model by comparison with other methods like FEM or ANCF.

Declaration of competing interest

The authors declare that they have no known competing financial interests or personal relationships that could have appeared to influence the work reported in this paper.

Appendix

Mass matrix

The mass matrix $\boldsymbol{M}(\boldsymbol{q})$ mentioned in Eq. (12) is expanded as follows. The matrix is symmetric, so the lower triangular part has been omitted.

$$\boldsymbol{M}(\boldsymbol{q}) = \begin{bmatrix} nmL & M_{s\phi_1} & \cdots & M_{s\phi_n} & M_{s\psi_1} & \cdots & M_{s\psi_n} \\ & M_{\phi_{1,1}} & \cdots & M_{\phi_{1,n}} & M_{\phi\psi_{1,1}} & \cdots & M_{\phi\psi_{1,n}} \\ & & \ddots & \vdots & \vdots & \ddots & \vdots \\ & & & M_{\phi_{n,n}} & M_{\phi\psi_{n,1}} & \cdots & M_{\phi\psi_{n,n}} \\ & & & & M_{\psi_{1,1}} & \cdots & M_{\psi_{1,n}} \\ & & & & & \ddots & \vdots \\ & & & & & & M_{\psi_{n,n}} \end{bmatrix}$$

Using the same notation used above, we can specify the expression for the matrix entries:

$$M_{s\phi_j} = -(b_j m + M_{accd}) l \cos\psi_1 \cos\psi_j \sin\left(\phi_j - \phi_1\right)$$

$$M_{s\psi_j} = (b_j m + M_{accd}) l \left[\cos\psi_j \sin\psi_1 - \cos\psi_1 \sin\psi_j \cos\left(\phi_j - \phi_1\right)\right]$$

$$M_{\phi_{1,1}} = m\cos(\psi_1)^2 \left(c_i l^2 + 2b_i sl + ns^2\right) + M_{accd}\cos(\psi_1)^2 (l^2 + 2sl + s^2) + \frac{l^2}{12}$$

$$M_{\phi_{i=j,j\neq 1}} = \frac{ml^2}{12}\left(c_i \cos(\psi_i)^2 + 1\right) + M_{accd}\left(\cos\psi_1\right)^2 (l^2)$$

$$M_{\phi_{i,j}} = (b_j m + M_{accd})\, h_i\, l \cos\psi_i \cos\psi_j \cos\left(\phi_j - \phi_i\right)$$

$$M_{\phi\psi_{i,j}} = -(b_j m + M_{accd}) l\, h_i \cos\psi_i \sin\psi_j \sin\left(\phi_j - \phi_i\right)$$

$$M_{\psi_{i,j}} = \begin{cases} b_j\, ml^2 + 2b_i msl + nms^2 + M_{accd}\,(l^2 + 2sl + s^2) & \text{for } i = j = 1 \\ (b_j m + M_{accd})\, h_i\, ml\, \left[\cos\psi_i \cos\psi_j + \sin\psi_i \sin\psi_j \cos\left(\phi_j - \phi_i\right)\right] & \text{else} \end{cases}$$

The following notations were used to simplify the equations. The same expressions apply for i and j:

$$h_i = \begin{cases} l + s & \text{for } i = 1 \\ l & \text{else} \end{cases}$$

$$b_i = \frac{2(n-i)+1}{2}$$

$$c_i = \frac{3(n-i)+1}{3}$$

$$d_i = \frac{4(n-i)+1}{4}$$

Inertia forces

The inertia terms $(\boldsymbol{f})$ on the right hand side of Eq. (12) is expanded as follows: $\boldsymbol{f}(t, \boldsymbol{q}, \dot{\boldsymbol{q}}) = [f_s, f_{\phi_1}, \ldots, f_{\phi_n}, f_{\psi_1}, \ldots, f_{\psi_n}]$

$$\begin{aligned} f_s = {} & l\cos\psi_1 \sum_{j=2}^{n} (b_j m + M_{accd}) \cos\psi_j \cos\left(\phi_j - \phi_1\right)\left(\dot{\phi}_j{}^2 + \dot{\psi}_j{}^2\right) \\ & -2l\cos\psi_1 \sum_{j=2}^{n} (b_j m + M_{accd}) \sin\psi_j \sin\left(\phi_j - \phi_1\right)\dot{\phi}_j \dot{\psi}_j \\ & +\frac{l}{2}\sin\psi_1 \sum_{j=2}^{n} (b_j m + M_{accd}) \sin\psi_j\, \dot{\psi}_j{}^2 \\ & +\left(b_1 ml + nms\right)\left[\dot{\phi}_1{}^2 \left(\cos\psi_1\right)^2 + \dot{\psi}_1{}^2\right] \end{aligned}$$

$$\begin{aligned} f_{\phi_1} = {} & l\, h_1 \cos\psi_1 \sum_{j=2}^{n} (b_j m + M_{accd}) \cos\psi_j \sin\left(\phi_j - \phi_1\right)\left(\dot{\phi}_j{}^2 + \dot{\psi}_j{}^2\right) \\ & +2l\, h_1 \cos\psi_1 \sum_{j=2}^{n} (b_j m + M_{accd}) \sin\psi_j \cos\left(\phi_j - \phi_1\right)\dot{\phi}_j \dot{\psi}_j \\ & +2m\cos\psi_1 \sin\psi_1 \left(c_1 l^2 + 2b_1 sl + ns^2\right)\dot{\phi}_1 \dot{\psi}_1 \\ & -2m\left(\cos\psi_1\right)^2 \left(b_1 l + ns\right)\dot{s}\,\dot{\phi}_1 \end{aligned}$$

$$\begin{aligned} f_{\phi_i} = {} & l\cos\psi_i \sum_{j=2}^{n} h_j\,(b_j m + M_{accd}) \cos\psi_j \sin\left(\phi_j - \phi_i\right)\left(\dot{\phi}_j{}^2 + \dot{\psi}_j{}^2\right) \\ & +2l\cos\psi_i \sum_{j=2}^{n} h_j\,(b_j m + M_{accd}) \sin\psi_j \cos\left(\phi_j - \phi_i\right)\dot{\phi}_j \dot{\psi}_j \\ & +2b_i\, ml\cos\psi_i\, \dot{s}\left[\sin\psi_1 \sin\left(\phi_i - \phi_1\right)\dot{\psi}_1 - \cos\psi_1 \cos\left(\phi_i - \phi_1\right)\dot{\phi}_1\right] \\ & +2c_i ml^2 \cos\psi_i \sin\psi_i\, \dot{\phi}_i \dot{\psi}_i \end{aligned}$$

$$\begin{aligned} f_{\psi_1} = {} & -l\, h_1 \sin\psi_1 \sum_{j=2}^{n} (b_j m + M_{accd}) \cos\psi_j \cos\left(\phi_j - \phi_1\right)\left(\dot{\phi}_j{}^2 + \dot{\psi}_j{}^2\right) \\ & +2l\, h_1 \sin\psi_1 \sum_{j=2}^{n} (b_j m + M_{accd}) \sin\psi_j \sin\left(\phi_j - \phi_1\right)\dot{\phi}_j \dot{\psi}_j \\ & +ml\, h_1 \cos\psi_1 \sum_{j=2}^{n} b_j \sin\psi_j\, \dot{\psi}_j{}^2 \\ & -m\cos\psi_1 \sin\psi_1\, \dot{\phi}_1{}^2 \left(c_1 l^2 + 2b_1 sl + ns^2\right) \\ & -2m\left(b_1 l + ns\right)\dot{s}\,\dot{\psi}_1 \end{aligned}$$

$$
\begin{aligned}
f_{\psi_i} = \quad & -l \sin\psi_i \sum_{j=2}^{n} h_j \left(b_j m + M_{accd}\right) \cos\psi_j \cos\left(\phi_j - \phi_i\right) \left(\dot{\phi}_j{}^2 + \dot{\psi}_j{}^2\right) \\
& +2l \sin\psi_i \sum_{j=2}^{n} h_j \left(b_j m + M_{accd}\right) \sin\psi_j \sin\left(\phi_j - \phi_i\right) \dot{\phi}_j \dot{\psi}_j \\
& +l \cos\psi_i \sum_{j=2}^{n} \left(b_j m + M_{accd}\right) h_1 \sin\psi_j \, \dot{\psi}_j{}^2 \\
& +2b_i \, ml \sin\psi_i \, \dot{s} \left[\cos\psi_1 \sin\left(\phi_i - \phi_1\right) \dot{\phi}_1 - \sin\psi_1 \cos\left(\phi_i - \phi_1\right) \dot{\psi}_1\right] \\
& -2b_i \, ml \cos\psi_1 \cos\psi_i \, \dot{s} \, \dot{\psi}_1 \\
& -c_i ml^2 \cos\psi_i \sin\psi_i \, \dot{\phi}_j{}^2
\end{aligned}
$$

References

[1] M. Sippel, J. Klevanski, J. Kauffmann, Innovative method for return to the launch site of reusable winged stages, in: International Astronautical Congress, 2001.

[2] Verfahren zum bergen einer stufe eines mehrstufigen raumtransportsystems (DE 101 47 144 C1 2003).

[3] M. Sippel, S. Singh, S. Stappert, RLV-return mode "In-Air-Capturing" and definition of its development roadmap, in: 9th European Conference on Aeronautics and Space Sciences, EUCASS, 2022.

[4] S. Stappert, J. Wilken, L. Bussler, M. Sippel, Innovative method for return to the launch site of reusable winged stages, in: International Astronautical Congress, 2019.

[5] S. Stappert, J. Wilken, G.J.C. Dominguez, M. Sippel, Evaluation of parametric cost estimation in the preliminary design phase of reusable launch vehicles, in: 9th European Conference on Aeronautics and Space Sciences, EUCASS, 2022.

[6] S. Singh, M. Simioana, S. Stappert, M. Sippel, S. Buckingham, S. Lopes, Y.C. Kucukosman, Control design and analysis of a capturing device performing In-Air Capturing of a reusable launch vehicle, in: 9th European Conference on Aeronautics and Space Sciences, EUCASS, 2022.

[7] S. Singh, S. Stappert, S. Buckingham, S. Lopes, Y.C. Kucukosman, M. Simioana, P. Planquart, Dynamic modelling and control of an aerodynamically controlled capturing device for 'In-Air-Capturing'of a reusable launch vehicle, in: 11th International ESA Conference on Guidance, Navigation and Control Systems, 2021.

[8] S. Singh, S. Stappert, L. Bussler, M. Sippel, Y.C. Kucukosman, S. Buckingham, Full-scale simulation and analysis of formation flight during In-Air Capturing of a winged reusable launch vehicle, J. Space Saf. Eng. 9 (4) (2022) 541–552.

[9] S. Stappert, S. Singh, M. Sippel, Developing an innovative and high-performance method for recovering reusable launcher stages: The in-air-capturing method, CEAS Space J. (2023) http://dx.doi.org/10.1007/s12567-023-00512-0.

[10] L. Meirovitch, Fundamentals of Vibrations, Waveland Press, 2010.

[11] N. Lv, J. Liu, H. Xia, J. Ma, X. Yang, A review of techniques for modeling flexible cables, Comput. Aided Des. 122 (2020) 102826.

[12] Y.I. Choo, M.J. Casarella, A survey of analytical methods for dynamic simulation of cable-body systems, J. Hydronaut. 7 (4) (1973) 137–144.

[13] A.A. Shabana, Flexible multibody dynamics: review of past and recent developments, Multibody Syst. Dyn. 1 (1997) 189–222.

[14] J. Genin, S.J. Citron, R.R. Huffman, Coupling of longitudinal and transverse motions of a flexible cable in a uniform flow field, J. Acoust. Soc. Am. 52(1B) (1972) 438–440.

[15] J.W. Kamman, R.L. Huston, Modeling of variable length towed and tethered cable systems, J. Guid. Control Dyn. 22 (4) (1999) 602–608.

[16] J.W. Kamman, T.C. Nguyen, J.W. Crane, Modeling towed cable system dynamics, 1989.

[17] P. Williams, D. Sgarioto, P. Trivailo, Optimal control of an aircraft-towed flexible cable system, J. Guid. Control Dyn. 29 (2) (2006) 401–410.

[18] P. Williams, P. Trivailo, Dynamics of circularly towed aerial cable systems, part 2: Transitional flight and deployment control, J. Guid. Control Dyn. 30 (3) (2007) 766–779.

[19] L. Morozov, A technique of determining the wing geometry for an aircraft cable-towed by a carrier, Russ. Aeronaut. (Iz VUZ) 58 (2015) 100–105.

[20] M. Song, F. Zhang, B. Huang, P. Huang, Enhanced anti-disturbance control for tethered aircraft system under input saturation and actuator faults, Nonlinear Dynam. 111 (22) (2023) 21037–21050.

[21] W. Ribbens, F. Saggio, R. Wierenga, M. Feldmann, Dynamic modeling of an aerial refueling hose and drogue system, in: 25th AIAA Applied Aerodynamics Conference, 2007.

[22] K. Ro, J.W. Kamman, Dynamics of circularly towed aerial cable systems, part 2: Transitional flight and deployment control, J. Guid. Control Dyn. 33 (1) (2010) 53–63.

[23] H. Wang, X. Dong, J. Xue, J. Liu, Dynamic modeling of a hose-drogue aerial refueling system and integral sliding mode backstepping control for the hose whipping phenomenon, Chin. J. Aeronaut. 27 (4) (2014) 930–946.

[24] Z.H. Zhu, S.A. Meguid, Elastodynamic analysis of aerial refueling hose using curved beam element, AIAA J. 44 (6) (2006) 1317–1324.

[25] Z.H. Zhu, S.A. Meguid, Modeling and simulation of aerial refueling by finite element method, Int. J. Solids Struct. 44 (24) (2007) 8057–8073.

[26] A.A. Shabana, An overview of the ANCF approach, justifications for its use, implementation issues, and future research directions, Multibody Syst. Dyn. 58 (2023) 433–477.

[27] A.A. Shabana, Dynamics of Multibody Systems, Cambridge University Press, 2020.

[28] P. Fritzkowski, H. Kamiński, Dynamics of a rope modeled as a multi-body system with elastic joints, Comput. Mech. 46 (2010) 901–909.

[29] P. Fritzkowski, H. Kamiński, Dynamics of a rope as a rigid multibody system, J. Mech. Mater. Struct. 3 (6) (2008) 1059–1075.

[30] P. Fritzkowski, H. Kamiński, A discrete model of a rope with bending stiffness or viscous damping, Acta Mech. Sin. 27 (2011) 108–113.

[31] M. Mastrogiuseppe, Student thesis: A multibody approach to modelling of rope dynamics, 2023.

[32] S. Stappert, J. Wilken, L. Bussler, M. Sippel, A systematic assessment and comparison of reusable first stage return options, in: 70th International Astronautical Congress, 2020.

[33] G. Norris, M. Wagner, Airbus A340 and A330 (Jetliner history), 2001.

[34] M. Sippel, J. Klevanski, Progresses in simulating the advanced in-air-capturing method, in: 5th International Conference on Launcher Technology, Missions, Control and Avionics, 2003.

[35] S. Singh, L. Bussler, S. Callsen, S. Stappert, S. Lopes, S. Buckingham, Control design and analysis of a capturing device performing In-Air Capturing of a reusable launch vehicle, in: 9th European Conference on Aeronautics and Space Sciences, EUCASS, 2022.

[36] Y.C. Kucukosman, S. Lopes, S. Buckingham, P. Planquart, S. Singh, L. Bussler, S. Stappert, M. Sippel, Aerodynamic characterization of in-air capturing vehicles using CFD simulations, in: 9th European Conference on Aeronautics and Space Sciences, EUCASS, 2022.

[37] D.C. Wilcox, Turbulence Modeling for CFD, Vol. 2, DCW industries La Canada, CA, 1998.

[38] F.S. Iglesias, A.F. López, Rayleigh damping parameters estimation using hammer impact tests, Mech. Syst. Signal Process. 135 (2020) 106391.

[39] Y. Yang, X. Wang, Z. Wu, Experimental study of vibration characteristics of FRP cables for long-span cable-stayed bridges, J. Bridge Eng. 20 (4) (2015) 04014074.

[40] C. Liu, Y.-F. Wei, H.-T. Qiu, J. Zhang, C.-J. Liu, Study on the rheological behaviors of UHMWPE/CA-MMT nanocomposite, Polym. Compos. 36 (1) (2015) 47–50.

[41] J.H. Lee, L. Karlsen, C.W. Lee, A method for improving the dynamic simulation efficiency of underwater flexible structures by implementing non-active points in modelling, ICES J. Mar. Sci. 65 (9) (2008) 1552–1558.

[42] P.H. Zipfel, Modeling and Simulation of Aerospace Vehicle Dynamics, AIAA, 2000.

[43] S. Singh, M. Sippel, S. Stappert, Full-scale simulations of 'In-Air Capturing' return mode for winged reusable launch vehicles, J. Phys. Conf. Ser. 2526 (1) (2023) 012114.

[44] Teufelberger, HyperTEN, Technical fiber rope, 2023, URL https://www.teufelberger.com/en/hyperten-technical-fiber-rope.html, https://www.teufelberger.com/en/hyperten-technical-fiber-rope.html, [Acccessed: 06 January 2024].

[45] T.E. Toolbox, Wire rope strength, 2023, URL https://www.engineeringtoolbox.com/wire-rope-strength-d_1518.html, https://www.engineeringtoolbox.com/wire-rope-strength-d_1518.html, [Acccessed: 06 January 2024].

[46] H.L. Stein, Ultra High Molecular Weight Polyethylene, UHMWPE, Engineering Materials Handbook, 1988.